PHYSICAL REVIEW B **92**, 174301 (2015)

Reflection thermal diffuse x-ray scattering for quantitative determination of phonon dispersion relations

A. B. Mei,[1] O. Hellman,[2] C. M. Schlepütz,[3,4] A. Rockett,[1] T.-C. Chiang,[5] L. Hultman,[6] I. Petrov,[1,6] and J. E. Greene[1,6]

[1]*Department of Materials Science and the Materials Research Laboratory, University of Illinois, 104 South Goodwin, Urbana, Illinois 61801, USA*

[2]*Department of Applied Physics and Materials Science, California Institute of Technology, Pasadena, California 91125, USA*

[3]*X-ray Science Division, Advanced Photon Source, Argonne National Laboratory, 9700 South Cass Avenue, Argonne, Illinois 60439, USA*

[4]*Swiss Light Source, Paul Scherrer Institut, 5232 Villigen PSI, Switzerland*

[5]*Department of Physics and the Materials Research Laboratory, University of Illinois, 1110 West Green Street, Urbana, Illinois 61801, USA*

[6]*Thin Film Physics Division, Department of Physics (IFM), Linköping University, SE-58183 Linköping, Sweden*

(Received 24 August 2015; revised manuscript received 1 October 2015; published 3 November 2015)

Synchrotron reflection x-ray thermal diffuse scattering (TDS) measurements, rather than previously reported transmission TDS, are carried out at room temperature and analyzed using a formalism based upon second-order interatomic force constants and long-range Coulomb interactions to obtain quantitative determinations of MgO phonon dispersion relations $\hbar\omega_j(\mathbf{q})$, phonon densities of states $g(\hbar\omega)$, and isochoric temperature-dependent vibrational heat capacities $c_v(T)$. We use MgO as a model system for investigating reflection TDS due to its harmonic behavior as well as its mechanical and dynamic stability. Resulting phonon dispersion relations and densities of states are found to be in good agreement with independent reports from inelastic neutron and x-ray scattering experiments. Temperature-dependent isochoric heat capacities $c_v(T)$, computed within the harmonic approximation from $\hbar\omega_j(\mathbf{q})$ values, increase with temperature from 0.4×10^{-4} eV/atom K at 100 K to 1.4×10^{-4} eV/atom K at 200 K and 1.9×10^{-4} eV/atom K at 300 K, in excellent agreement with isobaric heat capacity values $c_p(T)$ between 4 and 300 K. We anticipate that the experimental approach developed here will be valuable for determining vibrational properties of heteroepitaxial thin films since the use of grazing-incidence ($\theta \lesssim \theta_c$, where θ_c is the density-dependent critical angle) allows selective tuning of x-ray penetration depths to $\lesssim$10 nm.

DOI: 10.1103/PhysRevB.92.174301 PACS number(s): 63.20.−e, 63.20.dd, 63.20.dh

I. INTRODUCTION

Phonons, elementary quanta of lattice vibrations, are well known to control high-temperature transport and structural properties of crystalline solids [1–7]. As a result, the ability to spectrally resolve phonon energies has proven central to the understanding of fundamental materials properties. Techniques by which phonon energies $\hbar\omega_j$, in which $\hbar$ is the reduced Planck constant and ω_j the angular frequency of phonon branch j, may be obtained include Raman [8] and tunneling spectroscopy [9]. Often, however, crystal properties are strongly influenced by phonons with specific momenta; archetype examples are systems exhibiting charge density waves [2] and Kohn anomalies [1]. In such cases, a deeper understanding of crystalline properties requires determination of dispersion relations $\hbar\omega_j(\mathbf{q})$ in which both phonon momenta $\mathbf{q}$ and energies $\hbar\omega_j$ are resolved. Historically, $\hbar\omega_j(\mathbf{q})$ curves have been determined by inelastic x-ray and neutron scattering (INX and INS). These techniques, nevertheless, require complex experimental equipment, long acquisition times, and, in the case of neutron scattering, large single crystals. The latter restriction eliminates many interesting thin-film systems such as pseudomorphic heterostructures and metastable materials.

Recently, transmission thermal diffuse x-ray scattering (TDS) has become an efficient experimental alternative for determining phonon dispersion relations. Thermal diffuse x-ray scattering experiments involve the detection of x-ray photons which are quasielastically scattered from thermally excited atoms vibrating about their equilibrium position. Displaced atoms break the symmetry of the ideal crystal, resulting in scattering away from Bragg peaks. Atomic displacements accompanying zone-boundary X-point phonons in face-centered-cubic (fcc) materials, for example, yield an irreducible superstructure that is double the size of the ideal unit cell. As a result, TDS intensities due to X-point phonons appear halfway between Bragg reflections at reciprocal space positions described by mixed-integer Miller indices, e.g. [0 0 1] and [1 1 0]. Pioneering work by Holt *et al.*, Wong *et al.*, Holt *et al.*, and Xu *et al.* demonstrated the capabilities of TDS measurements by determining $\hbar\omega_j(\mathbf{q})$ phonon dispersion curves for Si [10], Ga-stabilized Pu [11], $TiSe_2$ [12], and Cu [13] crystals. However, TDS experiments are presently carried out in transmission geometry and, as a result, samples are limited to bulk crystals.

Thin films represent a technologically important class of materials for which the number of sample types is increasingly growing. In particular, novel metastable phases, inaccessible by bulk synthesis techniques, can be produced using kinetically limited growth processes [14–21] and epitaxial constraints [22–27]. Despite the importance of thin films, there are only a restricted number of methods [28,29] for determining phonon dispersion relations for this class of materials.

Here, we introduce a TDS technique for determining phonon dispersions $\hbar\omega_j(\mathbf{q})$ and densities of states $g(\hbar\omega)$ based on a reflection scattering configuration. We demonstrate the method using MgO as a model materials system. It is anticipated that the results presented here will be beneficial for selectively determining vibrational properties of heteroepitaxial thin films, since x-ray penetration depths may be tuned using grazing incidence geometries. From thermal-diffuse x-ray pole figures, we determine $\hbar\omega_j(\mathbf{q})$ and $g(\hbar\omega)$ and compute, via the harmonic approximation, temperature-dependent isochoric MgO heat capacities $c_v(T)$. MgO is chosen for this study due to its nearly harmonic behavior as well as its mechanical and dynamic stability [30]. Pole figures are measured about an 011 oriented sample normal, since this primary cubic direction exhibits lower symmetry, twofold, and, thus, allows the sampling of a higher number of unique reciprocal space points than the fourfold symmetric 001 and threefold symmetric 111 orientations.

II. EXPERIMENTAL PROCEDURES

Thermal-diffuse synchrotron x-ray pole figure measurements were collected at beamline 33-BM of the Advanced Photon Source, Argonne National Laboratory. Experiments were performed with the storage ring operating in top-up mode with an electron energy of 7 GeV and a stored current of 100 mA. Using a double-crystal Si(111) monochromator, the wavelength of the x-ray probe beam was set to 0.05904 nm (21 keV). Polished MgO(011) sample wafers, $5 \times 5\,\mathrm{mm}^2$, were obtained from the MTI Corporation. To minimize air scattering during measurements, samples were enclosed in a Be-dome-covered stage and evacuated to 1×10^{-6} Torr (1.3×10^{-4} Pa). Scattering from the Be-dome was eliminated by placing collimating slits close to the sample holder. The x-ray probe beam was focused onto the detector plane, yielding 1×10^{12} photons/s incident on an $800 \times 400\,\mu\mathrm{m}^2$ area of the sample surface. Beam divergence, which was almost exclusively in the horizontal plane of the synchrotron, was ~4 mrad and had a negligible effect on resolution when compared to the typical size of thermal diffuse features, spanning several degrees. All scattering experiments were performed in the vertical plane of the synchrotron to avoid polarization effects. Scattering intensities were recorded at each pixel of a Pilatus 100 K area detector to produce 400 individual pole figures over azimuthal angles $\chi = 0\text{–}80^\circ$ and rotational angles $\varphi = 0\text{–}360^\circ$, covering diffraction vectors ranging from $q = 42.60$ to $70.32\,\mathrm{nm}^{-1}$. The resulting data set encompasses over one million individually sampled reciprocal space points.

III. THEORETICAL PROCEDURES

A. MgO phonon dispersion relations

In order to obtain MgO phonon dispersion relations $\hbar\omega_j(\mathbf{q})$, phonon densities of states $g(\hbar\omega)$, and temperature-dependent vibrational heat capacities $c_v(T)$, thermal diffuse intensities were computed based on an 11-parameter Born-von-Karman model which incorporates short-range second-nearest-neighbor interatomic interactions and long-range Coulomb interactions. Model parameters, including MgO high-frequency dielectric constants, Born effective charges, and interatomic force constants, were then iteratively adjusted using a hybrid simulated annealing and robust nonlinear least-squares minimization routine until the best match between theoretical and experimental diffracted intensities was obtained. Simulated annealing is a stochastic metaheuristic optimization algorithm that searches for the global minimum, while avoiding local minima traps. Least-squares routines use Hessians to converge efficiently once the neighborhood of a global minimum is found.

MgO phonon dispersion relations $\hbar\omega_j(\mathbf{q})$ and phonon eigenvectors $\boldsymbol{\varepsilon}_j(\mathbf{q})$, corresponding to vibrational energies and atomic displacements associated with specific phonon wave vectors, were obtained by diagonalizing dynamical matrices $\mathbf{D}(\mathbf{q})$

$$\mathbf{D}(\mathbf{q})\boldsymbol{\varepsilon}_j(\mathbf{q}) = \omega_j^2(\mathbf{q})\boldsymbol{\varepsilon}_j(\mathbf{q}). \tag{1}$$

For crystals with n atoms in the primitive unit cell, $\mathbf{D}(\mathbf{q})$, $\boldsymbol{\varepsilon}_j(\mathbf{q})$, and $\omega_j^2(\mathbf{q})$ are matrices with dimensions $3n \times 3n$. In ionic crystals, such as MgO, dynamical matrices consist of two contributions

$$\mathbf{D}(\mathbf{q}) = \mathbf{D}_I(\mathbf{q}) + \mathbf{D}_C(\mathbf{q}). \tag{2}$$

$\mathbf{D_I}(\mathbf{q})$ describes short-range interatomic forces, and $\mathbf{D_C}(\mathbf{q})$ represents long-range Coulomb interactions. The elements of short-range dynamical matrices are obtained by Fourier transforming interatomic force constants Φ

$$\mathbf{D}_I(\mathbf{q}) \equiv \mathbf{D}_{ss'}^{\alpha\beta}(\mathbf{q}) = \frac{1}{\sqrt{\mu_s\mu_{s'}}}\sum_{m'}\Phi^{\alpha\beta}_{sms'm'}\exp[iq \cdot R_{mm'}]. \tag{3}$$

s and s' are indices of the two basis atoms in the primitive fcc unit cell, m and m' correspond to two different primitive unit cells, and α and β are two of the three Cartesian directions. μ_s is the mass of atom s, and $R_{mm'}$ is the distance between unit cells m and m'. To reproduce MgO atomic vibrations with the smallest number of parameters, we consider only second-nearest-neighbor interactions and employ full crystal symmetry operations. This reduces the number of interatomic force constants from over 800 to only eight independent values.

In the continuum limit (i.e. $q \simeq 0$), Cochran and Cowley [31] showed that the long-range dynamical matrix, which describes Coulomb interactions and gives rise to Lyddane-Sachs-Teller [32] splitting of transverse and longitudinal optical phonon modes (TO and LO), reduces to

$$\tilde{\mathbf{D}}_\mathrm{C}(\mathbf{q}) = \frac{e^2}{\varepsilon_o V}\frac{[\mathbf{q}\,\mathbf{Z}^*(s)]_\alpha[\mathbf{q}\,\mathbf{Z}^*(s')]_\beta}{\mathbf{q}\boldsymbol{\varepsilon}_\infty\mathbf{q}}. \tag{4}$$

$Z^*(s)$ is the Born effective charge tensor of atom s, $\boldsymbol{\varepsilon}_\infty$ is the high-frequency dielectric tensor, ε_o is the permittivity of free space, e the electron charge, and V the unit-cell volume. For cubic materials, $\mathbf{Z}^*$ and $\boldsymbol{\varepsilon}_\infty$ are scaled identity matrices. In order to simulate the effect of Coulomb interactions throughout the Brillouin zone, long-range dynamical matrices are constructed using a Fourier interpolation scheme based on Cochran and Cowley's results [33]

$$\mathbf{D}_\mathrm{C}(\mathbf{q}) = \tilde{\mathbf{D}}_\mathrm{C}(\mathbf{q})\left\{\cos\left(\frac{|\mathbf{q}|}{q_{\max}}\right)^r\right\}. \tag{5}$$

The term in curly brackets is an interpolating function, $q_{\max}$ is the magnitude of the largest wave vector in the first Brillouin zone, and r is an empirical cutoff parameter describing the spread of the Coulomb interaction away from the zone center.

Together, Eqs. (1)–(4) fully describe the wave vector and energy dependence of all MgO lattice vibrations via 11 material parameters: the Born effective charge, the high-frequency dielectric constant, a Coulomb interaction cutoff parameter, and eight second-nearest-neighbor interatomic force constants.

B. TDS intensities

Thermal diffuse scattering intensities are computed using the relationship [10,34]

$$I(\mathbf{q}) = A\left[\frac{\hbar N I_e}{2}\sum_j \frac{1}{\hbar\omega_j(\mathbf{q})}\coth\left(\frac{\hbar\omega_j(\mathbf{q})}{2k_BT}\right)|F_j(\mathbf{q})|^2\right] + B, \tag{6}$$

in which N is the number of unit cells in the crystal, I_e the scattering intensity from a single electron [35], and k_B is Boltzmann's constant. The summation is carried out over phonon branch indices j. The term in square brackets corresponds to first-order TDS intensities; higher-order terms, together with Compton scattering effects [35,36], are included via the empirical parameter B. The scaling parameter A controls the relative strength of first-order diffuse scattering intensities. In the limit of small phonon energies $\hbar\omega_j(\mathbf{q})$, the hyperbolic cotangent term, describing the increasing phonon thermal population, increases as $2k_BT/\hbar\omega_j(\mathbf{q})$ causing the intensity to increase at wave vectors close to Γ Brillouin-zone centers, i.e. Bragg reflections, where low-energy phonons exist in large populations: $I(\mathbf{q}) \propto 1/[\hbar\omega_j(\mathbf{q})^2 + \beta]$. β accounts for the fact that the thermal population around Γ is always finite.

The structure factor for the jth phonon branch is

$$F_j(\mathbf{q}) = \sum_s \frac{f_s}{\sqrt{\mu_s}}\exp[-M_s(\mathbf{q})][\mathbf{q}\cdot\boldsymbol{\varepsilon}_{js}(\mathbf{q})]\exp(-i\mathbf{q}\cdot\boldsymbol{\tau}_s), \tag{7}$$

in which f_s, $\boldsymbol{\tau}_s$, and $M_s(\mathbf{q})$ are the atomic scattering factor, atomic coordinates, and Debye-Waller factor of atom s [35]. $\boldsymbol{\varepsilon}_{js}(\mathbf{q})$ is the component of the eigenvector corresponding to atom s and phonon j.

Thus, MgO thermal-diffuse pole figure intensities depend on an 11-parameter model, Eqs. (1)–(5), and two empirical parameters, A and B. By comparing computed thermal-diffuse pole figure intensities to measured values and refining the parameters until the best fit between measured and simulated values is obtained, MgO vibrational properties, including phonon dispersion relations and temperature-dependent isochoric heat capacities, are determined. All subsequent discussion and results are based on the refined material parameters.

IV. RESULTS AND DISCUSSION

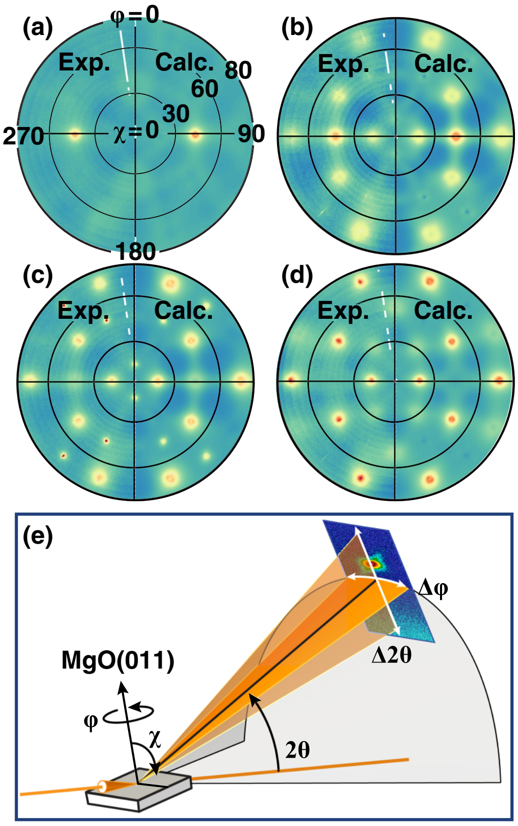

FIG. 1. (Color online) MgO(011) thermal-diffuse x-ray pole figures acquired with scattering vector q equal to (a) 57.82, (b) 62.61, (c) 64.42, (d) and 68.58 nm^{-1}. The pole figures are plotted as normalized logarithmic isointensity maps over azimuthal angles $\chi = 0{-}80^\circ$ and polar angles $\varphi = 0{-}360^\circ$. The left side of each pole figure ($180 < \varphi < 360^\circ$) is determined using synchrotron radiation; the right side ($0 < \varphi < 180^\circ$) is computed from theoretical MgO phonon dispersion relations obtained by fitting experimentally measured thermal-diffuse intensities, including those shown on the left side of each pole figure, to a model based on second-nearest-neighbor interatomic forces and long-range Columbic interactions. (e) An illustration defining azimuthal χ, rotational φ, and Bragg 2θ angles with respect to the MgO crystal and an area detector.

Typical synchrotron x-ray diffraction pole figures acquired from MgO(011) over the range $\varphi = 180{-}360^\circ$ with diffracting-vector magnitudes $q = 57.82, 62.61, 64.42,$ and $68.58\,\mathrm{nm}^{-1}$ are presented in Figs. 1(a)–1(d) as stereographic projections with logarithmically scaled diffracted intensities corrected for defocus [37–39]. The experimental geometry is defined in Fig. 1(e). Simulated thermal-diffuse intensities based on refined model parameters, which include descriptions of interatomic forces and Coulomb interactions, are plotted, for comparison, over rotational angles $\varphi = 0{-}180^\circ$ in Figs. 1(a)–1(d). Pole figures from 011-oriented cubic crystals are twofold symmetric about the vertical φ axis. Reciprocal space regions probed in Figs. 1(a)–1(d) are sufficiently distant from Brillouin-zone centers to avoid Bragg reflections and provide diffracted intensities that arise predominately from atomic vibrations. MgO(011) pole figures are acquired with $q = 57.82\,\mathrm{nm}^{-1}$ and shown in Fig. 1(a) to exhibit two strong diamond-shaped features ($\chi = 45; \varphi = 90, 270^\circ$) and two diffuse triangular features ($\chi = 35; \varphi = 0, 180^\circ$), which arise from thermal acoustic excitations around 002 and 111 Brillouin zone centers [40]. For $q = 62.61\,\mathrm{nm}^{-1}$, intensities weaken slightly near 002 and become more diffuse around 111; in addition, 10 features appear near 240 zone centers. With increasing q from 64.42 to $68.58\,\mathrm{nm}^{-1}$, Figs. 1(c) and 1(d), thermal diffuse intensities around 002 zone centers continue to decrease. In Fig. 1(c), 10 small features appear near 313 zone centers; 10 additional features appear near 242 zone centers in Fig. 1(d). Extracted profiles from measured and simulated thermal diffuse intensities acquired with $q = 68.58\,\mathrm{nm}^{-1}$,

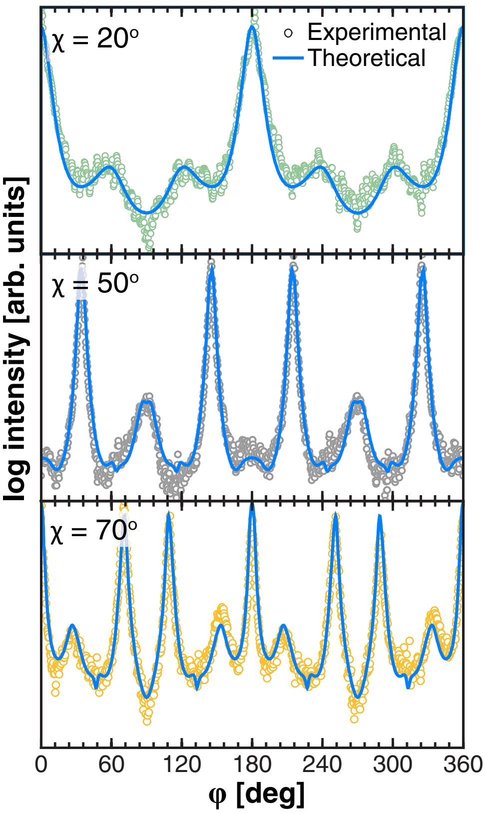

FIG. 2. (Color online) Typical MgO synchrotron thermal-diffuse x-ray intensity profiles (circles), plotted as a function of φ between 0 and 360° with $\chi = 20$, 50, and 70°, obtained from the pole figure shown in Fig. 1(d) acquired at scattering vector $q = 68.58\,\text{nm}^{-1}$. Simulated diffracted intensities (solid lines) calculated using MgO phonon dispersion relations obtained by fitting the measured pole-figure intensities using a model based on second-nearest-neighbor interatomic forces and long-range Columbic interaction parameters.

Figure 1(d), over the range $\varphi = 0-360^\circ$ for $\chi = 20$, 50, and 70° are shown on a logarithmic scale in Fig. 2 to be in excellent agreement.

Figures 3(a)–3(f) show simulated contributions to thermal-diffuse pole-figure intensities at $q = 68.58\,\text{nm}^{-1}$ from each of the six MgO(011) phonon branches. The figures are obtained using Eq. (6) to simulate each mode separately. Thermal diffuse scattering intensities arising from the lowest-energy acoustic phonon branch are shown in Fig. 2(a) and the highest-energy optical phonon branch in Fig. 3(f). The sum of the pole-figure intensities from all six phonon branches yield the total thermal-diffuse pole-figure intensity presented in Fig. 1(d). Since phonons branches are sorted by their eigenvalues, discontinuities in pattern intensities arise from sharp changes in phonon eigenvectors at points in reciprocal space where phonon branches cross. Mathematically, this results from the dot product in Eq. (7); physically, this indicates that lattice vibrations only contribute to scattering if atoms are displaced with a nonzero component parallel to the scattering vector. Diffracted intensities are largest for the three lowest energy phonon modes, Figs. 3(a)–3(c).

MgO phonon dispersion curves, obtained by simulating thermal-diffuse pole-figure intensities and refining model parameters to match measured results, are plotted along high-symmetry reciprocal-space directions in Fig. 4(a). INS results from MgO crystals [41], shown for comparison, are in good agreement. MgO acoustic phonon energies increase linearly near Γ, the Brillouin-zone center (000), and saturate toward the X and L zone boundaries (001 and $\frac{1}{2}\,\frac{1}{2}\,\frac{1}{2}$). The increase near the zone center is greater for longitudinal acoustic phonons, indicating higher propagation group velocities than for transverse phonons. Transverse and longitudinal optical phonon energies, 50 and 90 meV, are distinct at the Γ-point due to long-range Coulomb interactions. While TO modes exhibit weak dispersion, i.e. their energies vary slowly throughout the Brillouin zone, the energies of LO modes decrease rapidly toward X and L zone boundaries. Along the $X\Gamma\,[0\zeta\zeta]$ reciprocal-space path, where phonon polarization vectors point along [100] or $[0\bar{1}1]$, both pairs of transverse acoustic and transverse optical phonon branches exhibit unique energies. Along $\Gamma X\,[00\zeta]$ and $\Gamma L\,[\zeta\zeta\zeta]$ paths, the polarization vectors point along symmetrically equivalent directions; as a result, the energies of the acoustic transverse modes, as well as the optical transverse modes, are degenerate.

The MgO phonon densities of states $g(\hbar\omega)$, representing the number of vibrational states per eV-atom, are computed using the relationship

$$g(\hbar\omega) = \frac{1}{N}\sum_j \delta(\hbar\omega_j - \hbar\omega), \tag{8}$$

in which δ is the Dirac delta function. Resulting $g(\hbar\omega)$ values are presented in Fig. 5 together with reported results from density functional theory (DFT) calculations [33] and INX [42] and INS [41] measurements. The curves are in good agreement. $g(\hbar\omega)$ exhibits three primary features centered near $\hbar\omega = 33$, 52, and 70 meV. These arise from van-Hove singularities in $\hbar\omega_j(\mathbf{q})$ curves, i.e. points in reciprocal space where phonons have small group velocities and branch energies are approximately constant as a function of wave vector.

Figure 6 shows isochoric MgO heat capacities $c_v(T)$ over the temperature range 10–400 K. Values are calculated within the harmonic approximation through the integral transform [1,2]

$$c_v(T) = \frac{k_B}{4}\int_0^\infty \left(\frac{\hbar\omega}{2k_BT}\right)^2 \text{csch}^2\left(\frac{\hbar\omega}{2k_BT}\right) g(\hbar\omega)d\hbar\omega \tag{9}$$

using refined MgO model parameters obtained by fitting room-temperature thermal-diffuse pole-figure intensities. The values obtained are in excellent agreement with reported temperature-dependent isobaric heat capacities $c_p(T)$ values plotted as squares [43] and circles [44–46] in Fig. 6. At low temperatures ($T < 50\,\text{K}$), for which only long-range acoustic phonons exhibiting linear dispersions are thermally excited, MgO heat capacities increase following a cubic power-law behavior: $c_v \propto T^3$. At higher temperatures, $c_v(T)$ approaches the classical equipartition value, $c_v = 3k_B = 2.58 \times 10^{-4}\,\text{eV}/(\text{atom K})$. For $T = 400\,\text{K}$, the MgO heat capacity is 85% of the equipartition value, for $T = 1700\,\text{K}$, 99%. MgO melts at 3125 K. The fact that MgO heat capacities evaluated at constant volume and measured at constant pressures agree

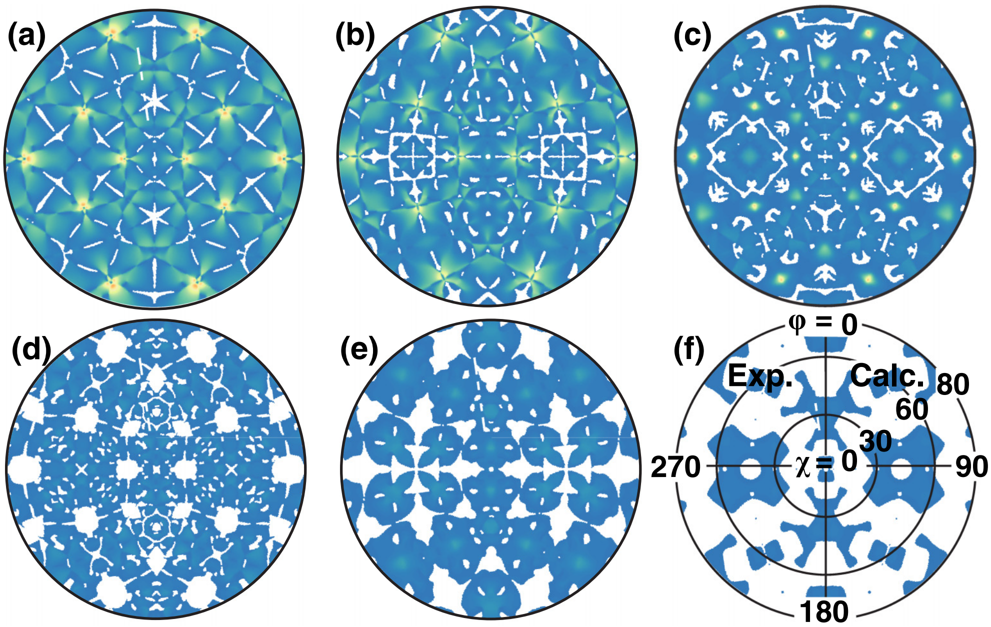

FIG. 3. (Color online) Simulated individual contributions from each phonon branch to MgO(011) thermal-diffuse pole-figure intensities acquired with scattering vector $q = 68.58\,\mathrm{nm}^{-1}$. The panels (a)–(f) are in order of increasing phonon energy, with (a) corresponding to the lowest acoustic phonon branch, and (f) the highest optical branch. Plots are presented as logarithmic isointensity maps over azimuthal angles $\chi = 0{-}80^\circ$ and rotational angles $\varphi = 0{-}360^\circ$. The sum of intensities in (a)–(f) yields the diffracted thermal-diffuse intensity pole-figure plot shown Fig. 1(d).

indicates that anharmonic effects, including those resulting from thermal expansion, are negligible at $T < 400\,\mathrm{K}$.

As a final point, we consider extending TDS to the analysis of thin films. Since TDS measurements are not constrained to specific scattering conditions, such as those fulfilling Bragg criteria, sensitivity to surface layers can be achieved by performing asymmetric grazing incidence measurements in which the x-ray beam is fixed at subcritical incidence angles with respect to the sample and diffuse scattering intensities are mapped in reciprocal space by moving only the detector. The x-ray/sample interaction volume is defined by α_i, the angle between the incident x-ray beam and the surface plane. For $\alpha_i < \theta_c$, the critical x-ray angle, total external reflection occurs resulting in evanescent waves which penetrate only very shallow subsurface regions. θ_c depends on the electron density of the exposed layer and the x-ray energy. For 21 keV x-rays

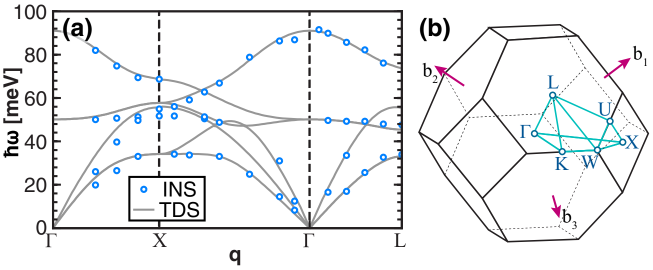

FIG. 4. (Color online) (a) MgO phonon dispersion relations (solid lines) obtained by fitting synchrotron reflection x-ray diffraction thermal-diffuse pole-figure intensities (Figs. 1–2) using a model based upon second-order-interatomic forces and long-range Coulomb interactions. Points from INS experiments, Ref. [41], are plotted for comparison. (b) The first Brillouin zone of MgO showing high symmetry points corresponding to $\Gamma[000]$, $X[100]$, $L[\frac{1}{2}\frac{1}{2}\frac{1}{2}]$, $W[\frac{1}{2}10]$, $U[\frac{1}{4}\frac{1}{4}]$, and $K[\frac{3}{4}\frac{3}{4}0]$. Indices are in units of $2\pi/a$ in which a is the MgO lattice parameter. b_1, b_2, and b_3 are reciprocal lattice vectors.

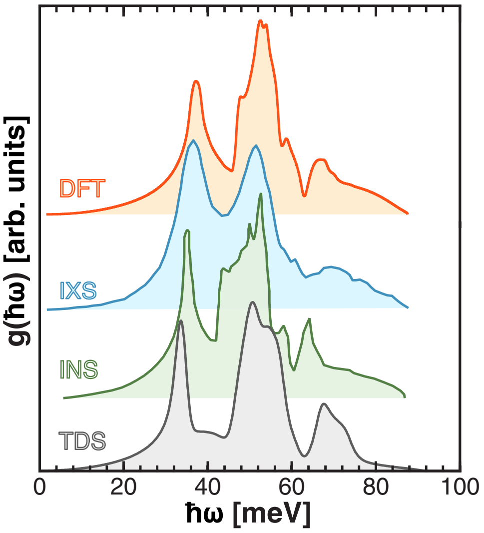

FIG. 5. (Color online) MgO phonon density of states $g(\hbar\omega)$ (black line, lower TDS curve) obtained by fitting synchrotron x-ray diffraction thermal-diffuse pole-figure intensities (Figs. 1–2) using a model based on second-order-interatomic forces and long-range Coulomb interactions. For comparison, $g(\hbar\omega)$ curves from inelastic neutron scattering experiments (green line, lower-middle INS curve) [41], inelastic x-ray scattering measurements (blue line, upper-middle INX curve) [42], and density functional theory calculations (red line, upper DFT curve) [33] are also shown.

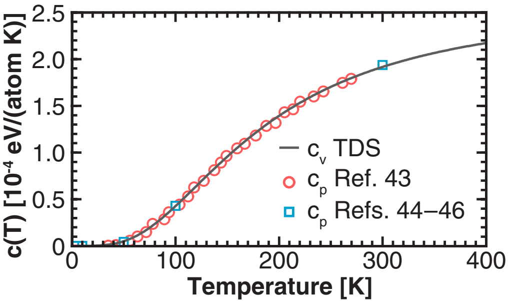

FIG. 6. (Color online) Temperature-dependent MgO isochoric heat capacities $c_v(T)$ (solid line) obtained by fitting synchrotron x-ray diffraction thermal-diffuse pole-figure intensities (Figs. 1–2), obtained at room-temperature, using a model based upon second-order interatomic forces and long-range Coulomb interactions. Squares and circles are isobaric heat capacities $c_p(T)$ from Refs. [43] and [44–46], respectively.

($\lambda = 0.05904$ nm) impinging on MgO, $\theta_c = 0.10^\circ$, yielding a penetration depth of $\lesssim 10$ nm at $\theta = 0.09^\circ$.

Even with a fixed α_i angle, it is possible to investigate vast regions of reciprocal space by moving the detector. This is illustrated by the following pair of equations which define the relationship between the incident α_i and outgoing α_f angles with respect to the surface plane, i.e. the real-space experimental arrangement, and the in-plane q_x and out-of-plane q_z reciprocal-space wave vector components [47,48]: $q_x = [\cos(\alpha_f) - \cos(\alpha_i)]/\lambda$ and $q_z = [\sin(\alpha_f) + \sin(\alpha_i)]/\lambda$. Equivalently, in terms of a Bragg-Brentano configuration, $\omega = \alpha_i$ and $2\theta = (\alpha_i + \alpha_f)$, $q_x = 2\sin(\theta)\sin(\theta - \omega)/\lambda$ and $q_z = 2\sin(\theta)\cos(\theta - \omega)/\lambda$. Thus, comprehensive data sets which sample thermal diffuse scattering intensities over wide regions of reciprocal space with fixed x-ray/sample interaction volume and selective surface sensitivity may be obtained and analyzed using the methods described above to quantitatively determine phonon dispersion relations for thin films with thicknesses as small as ∼10 nm.

V. CONCLUSIONS

We have demonstrated a method for determining phonon dispersion relations $\hbar\omega_j(\mathbf{q})$, phonon densities of states $g(\hbar\omega)$, and temperature-dependent vibrational heat capacities $c_v(T)$ of solids based upon synchrotron TDS pole-figure measurements carried out in the reflection, rather than the previously investigated transmission, geometry. We anticipate that the experimental techniques presented here will be valuable for determining vibrational properties of heteroepitaxial thin films since x-ray penetration depths can be selectively tuned using grazing incidence. In order to illustrate the method, MgO was used as a model materials system due to its harmonic behavior and its high mechanical and dynamic stability. Resulting MgO phonon dispersion relations and densities of states were found to be in good agreement with independent reports from inelastic neutron and x-ray scattering experiments carried out on single crystals. Temperature-dependent heat capacities obtained within the harmonic approximation at constant volume agree with values measured at constant pressure between 4 and 300 K.

ACKNOWLEDGMENTS

The authors thank Dr. Mauro Sardela for valuable discussions. The financial support of the Swedish Research Council (VR) Grant No. 2014-5790 (Greene) and No. 2013-4018 (Hultman), the Swedish Government Strategic Research Area (SFO) Grant No. 2009-00971 in Materials Science on Advanced Functional Material (MatLiU AFM), and the US Department of Energy (DOE), Office of Science, Office of Basic Energy Sciences (TCC under Grant No. DE-FG02-07ER46383) is greatly appreciated. This research used resources of the Advanced Photon Source, a US DOE Office of Science User Facility operated for the DOE Office of Science by Argonne National Laboratory under Contract No. DE-AC02-06CH11357.

---

[1] N. W. Ashcroft and N. D. Mermin, *Solid State Physics*, 1st ed. (Brooks Cole, Pacific Grove, CA, 1976).

[2] C. Kittel, *Introduction to Solid State Physics*, 7th ed. (Wiley, Hoboken, NJ, 1995).

[3] M. Tinkham, *Introduction to Superconductivity*, 2nd ed. (Dover Publications, Mineola, NY, 2004).

[4] P. Phillips, *Advanced Solid State Physics*, 2nd ed. (Cambridge University Press, Cambridge, England, 2012).

[5] G. Rickayzen, *Green's Functions and Condensed Matter*, Reprint ed. (Dover Publications, Mineola, NY, 2013).

[6] A. B. Mei, O. Hellman, N. Wireklint, C. M. Schlepütz, D. G. Sangiovanni, B. Alling, A. Rockett, L. Hultman, I. Petrov, and J. E. Greene, Phys. Rev. B **91**, 054101 (2015).

[7] A. B. Mei, A. Rockett, L. Hultman, I. Petrov, and J. E. Greene, J. Appl. Phys. **114**, 193708 (2013).

[8] C. V. Raman and N. S. N. Nathe, Proc. Indian Acad. Sci. (Math. Sci.) **2**, 406 (1935).

[9] W. L. McMillan and J. M. Rowell, Phys. Rev. Lett. **14**, 108 (1965).

[10] M. Holt, Z. Wu, H. Hong, P. Zschack, P. Jemian, J. Tischler, H. Chen, and T.-C. Chiang, Phys. Rev. Lett. **83**, 3317 (1999).

[11] J. Wong, M. Wall, A. J. Schwartz, R. Xu, M. Holt, H. Hong, P. Zschack, and T.-C. Chiang, Appl. Phys. Lett. **84**, 3747 (2004).

[12] M. Holt, P. Zschack, H. Hong, M. Y. Chou, and T.-C. Chiang, Phys. Rev. Lett. **86**, 3799 (2001).

[13] R. Xu, H. Hong, P. Zschack, and T.-C. Chiang, Phys. Rev. Lett. **101**, 085504 (2008).

[14] B. M. Howe, E. Sammann, J. G. Wen, T. Spila, J. E. Greene, L. Hultman, and I. Petrov, Acta Mater. **59**, 421 (2011).

[15] H.-S. Seo, T.-Y. Lee, I. Petrov, J. E. Greene, and D. Gall, J. Appl. Phys. **97**, 083521 (2005).

[16] B. Howe, J. Bareno, M. Sardela, J. G. Wen, J. E. Greene, L. Hultman, A. A. Voevodin, and I. Petrov, Surf. Coat. Technol. **202**, 809 (2007).

[17] D. H. Mei, Y.-W. Kim, D. Lubben, I. M. Robertson, and J. E. Greene, Appl. Phys. Lett. **55**, 2649 (1989).

[18] P. Desjardins, T. Spila, O. Gürdal, N. Taylor, and J. E. Greene, Phys. Rev. B **60**, 15993 (1999).

[19] R. C. Powell, N.-E Lee, Y.-W Kim, and J. E. Greene, J. Appl. Phys. **73**, 189 (1993).

[20] F. Adibi, I. Petrov, L. Hultman, U. Wahlström, T. Shimizu, D. McIntyre, J. E. Greene, and J.-E Sundgren, J. Appl. Phys. **69**, 6437 (1991).

[21] I. Petrov, P. B. Barna, L. Hultman, and J. E. Greene, J. Vac. Sci. Technol., A **21**, S117 (2003).

[22] X. Y. Zhang, J. S. Chawla, R. P. Deng, and D. Gall, Phys. Rev. B **84**, 073101 (2011).

[23] D. Gall, C.-S. Shin, T. Spila, M. Odén, M. J. H. Senna, J. E. Greene, and I. Petrov, J. Appl. Phys. **91**, 3589 (2002).

[24] H. Luo, G. Zou, H. Wang, J. H. Lee, Y. Lin, H. Peng, Q. Lin, S. Deng, E. Bauer, T. M. McCleskey, A. K. Burrell, and Q. Jia, J. Phys. Chem. C **115**, 17880 (2011).

[25] Y. Zhang, N. Haberkorn, F. Ronning, H. Wang, N. A. Mara, M. Zhuo, L. Chen, J. H. Lee, K. J. Blackmore, E. Bauer, A. K. Burrell, T. M. McCleskey, M. E. Hawley, R. K. Schulze, L. Civale, T. Tajima, and Q. Jia, J. Am. Chem. Soc. **133**, 20735 (2011).

[26] I. Petrov, F. Adibi, J. E. Greene, W. D. Sproul, and W.-D. Munz, J. Vac. Sci. Technol., A **10**, 3283 (1992).

[27] J. E. Greene, J. Vac. Sci. Technol., B **1**, 229 (1983).

[28] G. Gopalakrishnan, M. V. Holt, K. M. McElhinny, J. W. Spalenka, D. A. Czaplewski, T. U. Schülli, and P. G. Evans, Phys. Rev. Lett. **110**, 205503 (2013).

[29] J. Serrano, A. Bosak, M. Krisch, F. J. Manjón, A. H. Romero, N. Garro, X. Wang, A. Yoshikawa, and M. Kuball, Phys. Rev. Lett. **106**, 205501 (2011).

[30] A. R. Oganov, M. J. Gillan, and G. D. Price, J. Chem. Phys. **118**, 10174 (2003).

[31] W. Cochran and R. A. Cowley, J. Phys. Chem. Solids **23**, 447 (1962).

[32] R. H. Lyddane, R. G. Sachs, and E. Teller, Phys. Rev. **59**, 673 (1941).

[33] Y. Wang, J. J. Wang, W. Y. Wang, Z. G. Mei, S. L. Shang, L. Q. Chen, and Z. K. Liu, J. Phys.: Condens. Matter **22**, 202201 (2010).

[34] M. Holt and T.-C. Chiang, Phys. Rev. Lett. **84**, 3734 (2000).

[35] B. E. Warren, *X-Ray Diffraction* (Courier Corporation, 1969).

[36] J. Als-Nielsen and D. McMorrow, *Elements of Modern X-Ray Physics*, 2nd ed. (Wiley, Hoboken, NJ, 2011).

[37] A. Segmüller, J. Appl. Phys. **43**, 2907 (1972).

[38] D. Wilson and D. W. Bainbridge, Metall. Trans. **2**, 2925 (1971).

[39] D. Chateigner, P. Germi, and M. Pernet, J. Appl. Crystallogr. **27**, 278 (1994).

[40] Bragg reflections are more localized than the diffuse TDS features. While the reciprocal space regions probed here are far from reciprocal lattice points relative to the width of Bragg reflections, the same regions may be close to reciprocal lattice points in comparison to the width of the diffuse TDS intensity. In addition, we adopt the convention of referring to reciprocal space directions, Brillouin-zone centers, and Bragg reflections by the corresponding lowest-integer Miller indices, i.e. [2 2 0] instead of [24 24 0]

[41] M. J. L. Sangster, G. Peckham, and D. H. Saunderson, J. Phys. C: Solid State Phys. **3**, 1026 (1970).

[42] A. Bosak and M. Krisch, Phys. Rev. B **72**, 224305 (2005).

[43] D. W. Cooke, F. Hellman, J. R. Groves, B. M. Clemens, S. Moyerman, and E. E. Fullerton, Rev. Sci. Instrum. **82**, 023908 (2011).

[44] O. Madelung, U. Rössler, and M. Schulz, Editors, *II-VI and I-VII Compounds; Semimagnetic Compounds* (Springer, Berlin, Germany, 1999), pp. 1.

[45] E. Gmelin, Cryogenics **7**, 225 (1967).

[46] E. Gmelin, J. Phys. Chem. Solids **30**, 2789 (1969).

[47] P. Ferraro, S. Grilli, and P. D. Natale, *Ferroelectric Crystals for Photonic Applications: Including Nanoscale Fabrication and Characterization Techniques* (Springer Science and Business Media, 2013).

[48] P. van der Sluis, J. Phys. D: Appl. Phys. **26**, A188 (1993).